JFM RAPIDS

Near-inertial wave propagation in a curved front

Ramana Patibandla[1] , **Christian E. Buckingham**[2] and **Amit Tandon**[1]

[1]University of Massachusetts Dartmouth, Old Westport Rd, North Dartmouth, MA, USA
[2]National Oceanography Center, European Way, Southampton SO14 3ZH, UK
Corresponding author: Amit Tandon, atandon@umassd.edu

In this work, we study the effect of flow curvature, or angular momentum, on the propagation and trapping characteristics of near-inertial waves (NIWs) in a curved front. The curved front is idealised as a baroclinic vortex in cyclogeostrophic balance. Motivated by ocean observations, we employ a Gaussian base flow, which by construction possesses a shield of oppositely signed vorticity surrounding its core, and we consider both cyclonic and anticyclonic representations of this flow. Following two main assumptions, i.e. that (i) the horizontal wavelength of the NIW is smaller than the length scale of the background flow (the WKBJ approximation), and (ii) the vertical wavelength of the NIW is smaller than the radial distance of interest, we derive the NIW dispersion relation and discuss the group velocity and direction of energy propagation. We show that the curvature can (i) increase the critical depth and horizontal extent of the trapping region, (ii) reduce NIW activity at the centre of the anticyclonic vortex core and enhance it in the cyclonic shield surrounding the core for high curvatures, (iii) lead to NIW trapping in the anticyclonic shield surrounding the cyclonic core, and (iv) increase the available band of NIW frequencies that are trapped. The solutions from the ray-tracing method are supported by numerical solutions of the governing equations linearised about the cyclogeostrophic base state. Finally, these methods are applied to an idealised model of oceanic mesoscale Arctic eddies showing an increase in the critical depth of trapping. Our results – while applied to polar eddies – equally apply at lower latitudes in both oceans and atmospheres, highlighting the potential importance of flow curvature in controlling the propagation of NIW energy.

Key words: internal waves, waves in rotating fluids

1. Introduction

Near-inertial waves (NIWs) are disturbances to the balanced flow in the ocean, with frequencies close to the inertial frequency ($f = 2\Omega \sin\theta$, where Ω is Earth's rotation rate, and θ is the latitude), with large horizontal and small vertical wavelength, generated

primarily by the wind stress (Alford *et al.* 2016). Due to their large vertical shear, they play a dominant role in vertical mixing (Wunsch & Ferrari 2004) and the oceanic energy budget (Munk & Wunsch 1998). The NIWs can interact energetically with the balanced flows and can act, interestingly, as an energy source and an energy sink for the balanced flow under different conditions (see Gertz & Straub 2009; Whitt & Thomas 2015; Taylor & Straub 2020; Thomas & Arun 2020; Thomas & Daniel 2021). Factors such as β-refraction (Gill 1984) and mean flow vorticity (ζ-refraction; Asselin & Young 2020) can modify the propagation characteristics of NIWs, among others. In the latter case, the geostrophic mean flow vorticity (ζ) reduces the local NIW frequency, 'trapping' NIWs in the anticyclonic regions – i.e. regions of negative (positive) ζ in the northern (southern) hemisphere – leading to their downward propagation and subsequent dissipation at a critical depth (Lee & Niiler 1998). Over the years, numerous observational studies reported concentrated NIW energy in anticyclonic regions (Perkins 1976; Elipot, Lumpkin & Prieto 2010; Voet *et al.* 2024), providing support for this theory. In the atmosphere, inertial-gravity waves are known to be generated from vortex dipoles and jets (Snyder *et al.* 2007; Wang, Zhang & Snyder 2009) and can interact with the balanced flows (Serafimovich *et al.* 2005; Niranjan Kumar *et al.* 2014).

Kunze (1985) showed NIW trapping using the Wentzel-Kramers-Brillouin-Jeffreys (WKBJ) approximation (i.e. the horizontal wavelengths of NIWs are considered to be smaller than the mean flow length scale) to derive the NIW dispersion relation. He showed that the lower bound of the NIW frequency band shifts to an effective Coriolis frequency given by $f_e = f\sqrt{1 + Ro_g} \approx f + \zeta/2$, where the approximation is valid for small-gradient Rossby numbers $Ro_g = \zeta/f$. Here, $\zeta(x, z)$ is the relative vorticity, while x and z are horizontal and vertical coordinates of a front, respectively. Using a ray-tracing approach in a model of barotropic and baroclinic jets, he demonstrated trapping of NIWs with frequencies $f_e < \omega < f$ in negative vorticity regions. It should be noted that the horizontal length scales of initial wind-generated NIWs are typically an order of magnitude larger than the geostrophic mean flow length scales, contrary to the aforementioned WKBJ approximation. For such a scenario, Young & Ben Jelloul (1997) developed a theory using multiple-scale analysis for a narrow band of NIWs with frequencies close to the inertial frequency; improvements on the theory have been reported in the subsequent literature (Thomas, Smith & Bühler 2017; Asselin & Young 2019). However, the WKBJ theory still provides an easier alternative to the latter in understanding NIW dynamics, their vertical propagation through ray tracing, and especially the location of the critical layer. For this reason, WKBJ theory and ray tracing have been employed frequently in observational studies (Kunze, Schmitt & Toole 1995; Lelong, Cuypers & Bouruet-Aubertot 2020; Xu *et al.* 2022). A recent study by Conn, Callies & Lawrence (2025) found that the WKBJ approach can be reconciled with the Young-Ben Jelloul (YBJ) method in the limit of weak-dispersiveness of NIW modes. Using a global plot of wave dispersiveness, they showed that high modes and high latitudes are weakly dispersive compared to low modes and mid/low latitudes, respectively (see for eg. Klein & Treguier 1994; Klein & Smith 2001).

Recently, Whitt & Thomas (2013) studied the effects of strong baroclinicity on NIW trapping in straight fronts using ray tracing, parcel arguments and numerical methods. They extended the aforementioned expression for the effective Coriolis frequency as $f_b = f\sqrt{1 + Ro_g - Ri_g^{-1}}$, where $Ri_g^{-1} = (\partial u_g/\partial z)^2/N^2$ is the inverse gradient Richardson number, $u_g(x, z)$ is the along-front geostrophic velocity of the background mean flow, and $N(x, z)$ is the buoyancy frequency. For strongly baroclinic fronts (i.e. large vertical shear), the lower bound of the NIWs can be reduced considerably. In addition, the horizontal and vertical extents of NIW propagation are shown to increase due to the baroclinicity

of the front. Using parcel arguments similar to those of Whitt & Thomas (2013), Joyce *et al.* (2013) derived an expression for the effective Coriolis frequency for NIWs in a baroclinic vortex, $f_c = f\sqrt{(1 + 2u_g/fr)(1 + Ro_g) - (1 + 2u_g/fr)^2 Ri_g^{-1}}$. Here, r is the radial distance from the centre of the vortex, and the term $2u_g/fr$, also defined as the local curvature number Cu, is due to the cyclogeostrophic balance of the mean flow, and indicates the importance of the centrifugal term over the Coriolis term and the extent of frontal curvature (Buckingham, Gula & Carton 2021*a*). It also scales as twice the ratio of centrifugal to Coriolis accelerations in the momentum equations (Shakespeare 2016). Although the expressions given by Whitt & Thomas (2013) and Joyce *et al.* (2013) have been used in observations and simulation works that study NIW propagation in anticyclonic eddies (Fer *et al.* 2018; Lelong *et al.* 2020; Essink *et al.* 2022; Kawaguchi *et al.* 2023), either the ray-tracing calculations implemented therein do not include the curvature term or the eddies considered therein correspond to small Rossby and curvature numbers. Works such as Llewellyn Smith (1999) and Kafiabad, Vanneste & Young (2021) studied NIW interaction in an anticyclonic vortex using the YBJ framework, again, at small Rossby numbers. The effect of the curvature term in the mean flow cyclogeostrophic balance has only been studied in Qu (2019) using ray-tracing theory in an idealised submesoscale vortex, and showed that the curvature term increases the critical depth of NIW trapping. However, the bulk curvature number (Cu_b, defined as the maximum of the local curvature number in the domain) considered in their study is -0.95.

To the best of our knowledge, the effect of the frontal curvature on NIW propagation over a wide parameter space ranging from straight fronts to highly curved fronts, with bulk curvature number magnitudes greater than 1, has not been explored yet. Therefore, in the current work, we use the WKBJ approximation, the ray-tracing approach and numerical methods to understand the modifications due to curvature in an idealised vortex that models a part of the curved front. Specifically, we focus on the propagation of sub-inertial waves in anticyclonic regions of both anticyclonic and cyclonic vortices. In § 2.1, we present the theory, the governing equation after the WKBJ approximation, the dispersion relation and group velocity expressions. In § 2.2, we describe the idealised vortex model used. In § 3, we discuss our findings from the ray-tracing theory. In § 4, we conclude by describing the implications of our findings by applying the ray-tracing method for typical Arctic sub-surface eddies. Validation of the ray-tracing theory using numerical solutions of the linearised governing equations has been provided in Appendix A.

2. Theory

2.1. *Dispersion relation and group velocity*

We consider a non-hydrostatic, Boussinesq flow on an f-plane composed of a mean state and a perturbation. The mean state is considered to be a curved oceanic front in a cyclogeostrophic balance, represented by an axisymmetric vortex with purely azimuthal flow. The velocity components, in cylindrical coordinates (r, θ, z), of the mean state flow are $(0, \bar{v}, 0)$. Here, r, θ and z are radial, azimuthal and axial coordinates, respectively. Note that due to axisymmetry, $\bar{v}$ is a function of only r and z. The governing equations for the mean state can be simplified into the cyclogeostrophic balance given by $\partial \bar{b}/\partial r = (f + 2\bar{v}/r)\,\partial \bar{v}/\partial z$, where $\bar{b}$ is the mean state buoyancy. The linearised governing equations for the perturbation quantities (u, v, w, P, b) are given by (Buckingham *et al.* 2021*a*)

$$\frac{\partial u}{\partial t} - \left(f + \frac{2\bar{v}}{r}\right)v = -\frac{\partial P}{\partial r}, \quad \frac{\partial v}{\partial t} + (f + \zeta)\,u + w\frac{\partial \bar{v}}{\partial z} = 0, \qquad (2.1a,b)$$

$$\frac{\partial w}{\partial t} - b = -\frac{\partial P}{\partial z}, \quad \frac{\partial b}{\partial t} + u\frac{\partial \bar{b}}{\partial r} + w\frac{\partial \bar{b}}{\partial z} = 0, \quad \frac{1}{r}\frac{\partial(ru)}{\partial r} + \frac{\partial w}{\partial z} = 0, \qquad (2.2a,b,c)$$

where, u, v and w are radial, azimuthal and axial velocities, respectively, $P = p/\rho_0$ is the pressure, ρ_0 is the reference density, b is the buoyancy, and $\zeta = \partial(r\bar{v})/r\,\partial r$ is the mean state vorticity. Note that the perturbation quantities are also assumed to be axisymmetric, therefore azimuthal derivatives $\partial/\partial\theta$ are neglected in (2.1)–(2.2). Although the gravest mode in a vortex is observed to be an azimuthal mode number -1 by Kunze *et al.* (1995), the axisymmetric assumption (i.e. azimuthal mode number 0) offers simplicity in applying the WKBJ approximation (e.g. Joyce *et al.* 2013; Conn *et al.* 2025). The amplitude of the perturbation velocities is assumed to be asymptotically smaller than the mean state velocity scale, so nonlinear terms of perturbation quantities can be ignored. One can therefore define a perturbation streamfunction as $u = \partial\psi/\partial z$ and $w = -(1/r)\,\partial(r\psi)/\partial r$. Assuming a normal mode form, $\psi \sim \Psi(r,z)\,e^{i\omega t}$, of the perturbation streamfunction and substituting in (2.1)–(2.2) yields, after simplification (Solberg 1936),

$$\left(N^2 - \omega^2\right)\left(\frac{\partial^2\Psi}{\partial r^2} + \frac{1}{r}\frac{\partial\Psi}{\partial r} - \frac{\Psi}{r^2}\right) - 2M^2\left(\frac{\partial^2\Psi}{\partial r\partial z} - \frac{1}{r}\frac{\partial\Psi}{\partial z}\right) + \left(\chi^2 - \omega^2\right)\frac{\partial^2\Psi}{\partial z^2} = 0,$$

$$(2.3)$$

where $N^2(r,z) = \partial\bar{b}/\partial z$ is the buoyancy frequency, $M^2(r,z) = \partial\bar{b}/\partial r$ is the baroclinic term, $\chi^2(r,z) = (f + 2\bar{v}/r)(f + \zeta)$ is the effective frequency, and ω is the intrinsic frequency. A non-zero $\partial\bar{b}/\partial r$ would imply a variation of density along constant pressure surfaces, and is the rationale behind calling it the 'baroclinic term' (Whitt & Thomas 2013). For perturbations of arbitrary length scales, (2.3) can be solved only numerically. Instead, noticing that the coefficients are also functions of r and z, one can obtain the region of wave propagation to be the region where the partial differential (2.3) is hyperbolic (see Whitt & Thomas 2013). The boundary of such a region is obtained by equating the discriminant of (2.3) to zero. For a given frequency ω, the wave propagation boundary is given by the contour

$$\omega_{min} := \sqrt{\frac{(N^2 + \chi^2) \pm \sqrt{(N^2 - \chi^2)^2 + 4M^4}}{2}} = \omega. \qquad (2.4)$$

Note that the expression ω_{min} here is a function of r and z, and so provides the minimum frequency that the background flow can support at a given spatial location. If the perturbations are also in a hydrostatic balance, (2.4) simplifies to $\omega_{min} := \sqrt{\chi^2 - M^4/N^2}$ as derived in Joyce *et al.* (2013) using parcel arguments. One can study the NIW propagation in such a region using the WKBJ approximation (Kunze 1985; Bender & Orszag 2013). As the region of interest is far from the centre of the vortex, one can set (following Brannigan *et al.* 2017) $r = r_0$ (a large quantity) in (2.3), which facilitates the use of the ansatz $\Psi \sim e^{i(kr+mz)}$. The resulting equation, to leading order in $1/mr_0$, leads to the dispersion relation (see Buckingham *et al.* 2021*a*)

$$\omega^2 = \frac{N^2 k^2 - 2M^2 km + \chi^2 m^2}{k^2 + m^2} = \frac{N^2\tau^2 - 2M^2\tau + \chi^2}{\tau^2 + 1}. \qquad (2.5)$$

Here, k and m are wavenumbers in the r and z directions, respectively, and $\tau = k/m$. Note that (2.5) is valid for radial distances $r \in (1/m, \infty)$. For a typical NIW vertical wavenumber $m \sim 10^{-2}$ m^{-1}, the lower limit is $O(100$ m$)$, a small number compared to typical radial length scales of $O(10$ km$)$. Moreover, as the vertical wavelength reduces further due to ζ-refraction, the aforementioned lower bound of applicability

reduces further. Given the dispersion relation (2.5), one can write the group velocity in the (r, z)-plane as $\boldsymbol{c}_g = (c_{gr}, c_{gz})$, where

$$c_{gr} = \frac{\partial \omega}{\partial k} = \frac{(N^2\tau + M^2(\tau^2 - 1) - \chi^2\tau)}{\omega m(\tau^2 + 1)^2}, \quad c_{gz} = \frac{\partial \omega}{\partial m} = -\tau c_{gr}. \tag{2.6}$$

Equations (2.5)–(2.6) can now be used to study ray paths in the aforementioned region of wave propagation. The ray-tracing equations are given by (Lighthill 2001)

$$\frac{\mathrm{d}k}{\mathrm{d}t} = -\frac{\partial \omega}{\partial r}, \quad \frac{\mathrm{d}m}{\mathrm{d}t} = -\frac{\partial \omega}{\partial z}, \quad \frac{\mathrm{d}r}{\mathrm{d}t} = c_{gr}, \quad \frac{\mathrm{d}z}{\mathrm{d}t} = c_{gz}. \tag{2.7}$$

We solve the aforementioned equations numerically. Note that the intrinsic frequency ω is constant along a ray path. The slope of a ray, describing the direction of the energy propagation, is given by $\mathrm{d}z/\mathrm{d}r = c_{gz}/c_{gr} = -\tau$. For a given intrinsic frequency $\omega = \omega_0$, τ can be obtained by solving the quadratic equation in (2.5) as

$$\tau(r, z) = \frac{M^2}{(N^2 - \omega_0^2)} \pm \frac{\sqrt{(\omega_0^2 - \omega_{min}^2)(\omega_0^2 + \omega_{min}^2 - (N^2 + \chi^2))}}{(N^2 - \omega_0^2)}. \tag{2.8}$$

Interestingly, this shows that if $\omega_{min} = \omega_0$, then the group velocity vector has slope $-M^2/(N^2 - \omega_0^2)$, although substituting (2.8) in (2.6) shows that the group velocity magnitude vanishes at $\omega_{min} = \omega_0$. If the perturbations are hydrostatic, then it reduces to $-M^2/N^2 = -(\partial\bar{b}/\partial r)/(\partial\bar{b}/\partial z)$ i.e. the isopycnal slope as described in Whitt & Thomas (2013). In other words, the NIW energy propagation is nearly aligned with the isopycnals close to the wave propagation boundary. The deviation from isopycnal slope depends on non-hydrostacy. Moreover, rays cannot propagate past the boundary as the group velocity vanishes, and thus encounter a turning point (where they reflect) or a critical point (where they stall) at the boundary (Bender & Orszag 2013).

2.2. *An idealised vortex flow*

In the current study, the mean state is considered to be a portion of a curved oceanic front represented by an idealised vortex. A vortex with positive vorticity in the core represents a front with positive curvature, and vice versa. Further, one can represent a straight front at one end in the limit $r \to \infty$, and a highly curved front on the other, for small, finite r. To describe the parameter space of curvature, a non-dimensional number termed the 'bulk curvature number' (Cu_b), as defined in the Introduction, can be used. It represents the relative importance of centrifugal and Coriolis forces in the momentum equations (Shakespeare 2016; Buckingham *et al.* 2021*a*). A small bulk curvature number $(|Cu_b| \ll 1)$ indicates a nearly straight front accurately described by geostrophic balance. In contrast, a large bulk curvature number $(|Cu_b| \gg 1)$ indicates a highly curved front better described by a cyclogeostrophic balance.

In addition to the above, we choose the vortex to be surrounded by a region of opposite vorticity (i.e. a shield) similar to the realistic scenarios (Kunze 1985). A class of Gaussian vortices defined based on pressure or density is used in literature (Mahdinia *et al.* 2017; Essink *et al.* 2022). However, by construction, such models cannot attain bulk curvature numbers less than -1, and so cannot be used to explore the wider curvature number space. Qu (2019) defined a vortex using trigonometric functions that contains a shield of opposite vorticity surrounding the core. However, the corresponding vorticity in the shield exhibits a non-physical divergence at the boundaries. In the current study, we consider a class of generalised Gaussian shielded vortices (termed 'CLM vortices') defined directly by
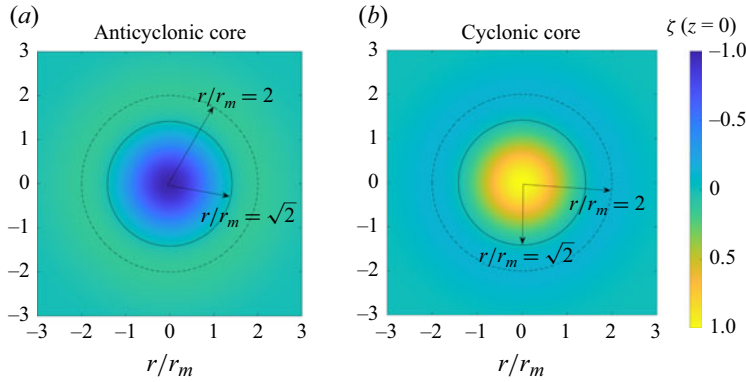
Figure 1. Contour plots of normalised vorticity (i.e. $\zeta r_m/2v_m$) in the $z = 0$ plane for (a) an anticyclonic vortex, and (b) a cyclonic vortex, showing a core region surrounded by a shield of opposite vorticity. The core region ends at $r/r_m = \sqrt{2}$. The relative vorticity magnitude in the shield attains a maximum at $r/r_m = 2$.

specifying the azimuthal velocity (Carton & McWilliams 1989; Buckingham *et al.* 2021*b*). The corresponding azimuthal velocity and relative vorticity expressions are given by

$$\left.\begin{array}{l} \bar{v}(r, z) = v_m \left(\dfrac{r}{r_m}\right) \exp\left(-\dfrac{1}{2}\dfrac{r^\alpha}{r_m^\alpha}\right) \exp\left(-\dfrac{(z - z_0)^2}{h^2}\right), \\[4mm] \zeta(r, z) = \dfrac{2v_m}{r_m} \left(1 - \dfrac{\alpha}{4}\dfrac{r^\alpha}{r_m^\alpha}\right) \exp\left(-\dfrac{1}{2}\dfrac{r^\alpha}{r_m^\alpha}\right) \exp\left(-\dfrac{(z - z_0)^2}{h^2}\right), \end{array}\right\} \quad (2.9)$$

where v_m is a characteristic velocity, r_m is the characteristic radius of the vortex, z_0 is the depth of the vortex centre, h is the e-folding length, and N_b is the background buoyancy frequency. A positive v_m implies a cyclonic vorticity in the core, and a negative v_m implies an anticyclonic vorticity in the core. In the current study, typical submesoscale vortices are chosen, i.e. $z_0 = 0$, $h = 100$ m and $\alpha = 2$. The expression for buoyancy ($\bar{b}$) can be obtained, by integrating the cyclogeostrophic balance for the above specified parameters, as $\bar{b}(r, z) = 2\bar{v}(fr + \bar{v})r_m^2 z/r^2 h^2 + N_b^2 z$. Here, the first term is due to the vortex flow field. The second term is due to the integration and is a function of z alone. Hence N_b^2 signifies a 'background' buoyancy gradient that is separate from the vortex and is considered a constant here for simplicity. Note that depending on $\bar{v}$, the buoyancy gradient $N^2 = \partial \bar{b}/\partial z = N_b^2 + N_v^2$ can attain negative values somewhere in the domain, when the buoyancy gradient due to the vortex flow field N_v^2 is negative and larger than N_b^2 in magnitude, implying a gravitational instability. To avoid such a scenario, we choose the background stratification to be sufficiently large (specifically, $N_b = 450f$) so that N^2 is always positive. Finally, for the CLM vortex model defined above, the bulk curvature number takes the form $Cu_b = 2v_m/fr_m$. Therefore, Cu_b could alternatively be called a 'vortex Rossby number' for the specific case of the CLM vortex model.

Below, we present ray-tracing and minimum frequency results for two CLM vortices: (i) anticyclonic vorticity in the core (or cyclonic vorticity in the shield), and (ii) cyclonic vorticity in the core (or anticyclonic vorticity in the shield). Figure 1 shows the contour plot of normalised vorticity, in both cases, plotted on a $z = 0$ plane. As depicted, the core region ends at $r/r_m = \sqrt{2}$ and is surrounded by a region of opposite vorticity, i.e. a shield. The magnitude of vorticity in the shield attains a maximum at $r/r_m = 2$. Note that the subsequent results, although for the CLM vortex model, have been checked with other idealised shielded vortex models (such as a shielded Rankine vortex and a
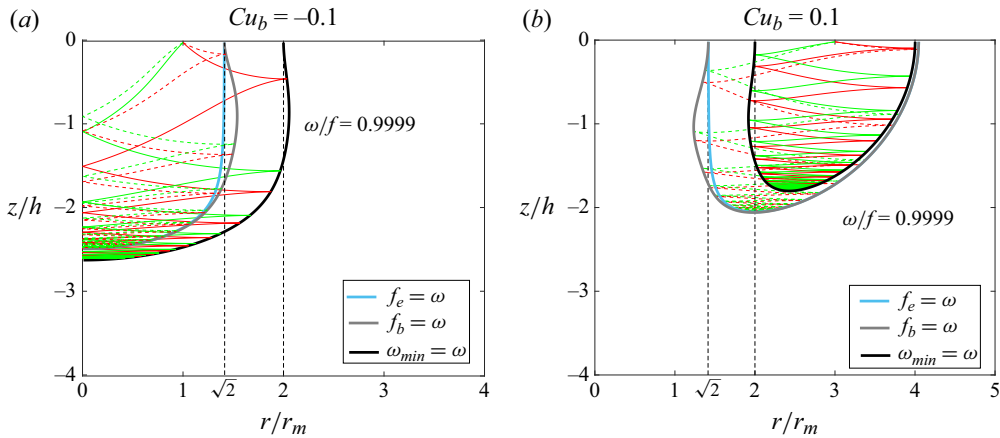
Figure 2. Downward-propagating rays (red and green curves) in (*a*) anticyclonic vortex, and (*b*) cyclonic vortex, at small curvature numbers ($|Cu_b| = 0.1$) and frequency $\omega/f = 0.9999$. The dashed curves are rays without curvature terms in the dispersion relation, while the continuous curves are rays with curvature term. Pale grey and black solid lines represent the boundary of wave propagation calculated from the effective frequency expressions f_e (i.e. non-baroclinic, non-curved scenario), f_b (i.e. geostrophic scenario) and ω_{min} (i.e. cyclogeostrophic scenario, see (2.4)), respectively. Here, we choose $v_m = \pm 0.5 \text{ m s}^{-1}$ and $r_m = 100$ km.

Mahdinia *et al.* (2017) vortex). The results are found to be in qualitative agreement among all the vortex models tested.

3. Ray-tracing and wave propagation characteristics

Consider effects of curvature on NIW propagation using ray-tracing analysis and minimum frequency expression (2.4). Figures 2(*a*) and 2(*b*) show the downward-propagating rays (red and green continuous curves) in both anticyclonic and cyclonic core vortices, for curvature number $|Cu_b| = 0.1$. For such small $|Cu_b|$, it is instructive to do the ray-tracing analysis by first neglecting the curvature term (i.e. $2\bar{v}/r$) in the dispersion relation and (2.1), and considering just the baroclinic contribution (dashed lines in figure 2*a*,*b*). The rays are initialised at $(r, z) = (r_m, -0.02h)$ in the anticyclonic core (figure 2*a*), and at $(r, z) = (3r_m, -0.02h)$ in the anticyclonic shield (i.e. the cyclonic core case, figure 2*b*) with frequency $\omega = 0.9999 f$. The reason for choosing a frequency so close to f is to show a common NIW frequency among all the plots. Figure 2(*a*) shows that NIWs propagate downwards in the core region of anticyclonic vorticity, as expected (Lee & Niiler 1998), reflecting at the boundary (i.e. at the turning points) given by (2.4), and approaching a critical point at a critical depth (Whitt & Thomas 2013). Figure 2(*b*) demonstrates that NIWs can propagate downwards and become trapped within the shield surrounding the cyclonic core, as well, an outcome and consideration that we believe is new to the oceanographic literature. It is evident from figure 2(*a*) that the rays considering the curvature term are steeper than the rays with baroclinic terms only. However, in figure 2(*b*), the rays are shallower with the inclusion of curvature terms. This contrasting behaviour can be understood from finding the contribution of the curvature terms to the wavevector direction (2.8). As the starting point of the ray is close to $z = 0$, one can simplify (2.8) by substituting $z = 0$, to obtain $\tau^2(r, z = 0) = (\omega_0^2 - \chi^2)/(N^2 - \omega_0^2)$. An immediate result, by noting that $\chi^2 = (f + 2\bar{v}/r)(f + \zeta)$, is that the contribution of the curvature term $2\bar{v}/r$ is to increase $|\tau|$ in the anticyclonic core, and decrease $|\tau|$ in the anticyclonic shield, thereby increasing the ray slope in figure 2(*a*) when compared to the purely geostrophic
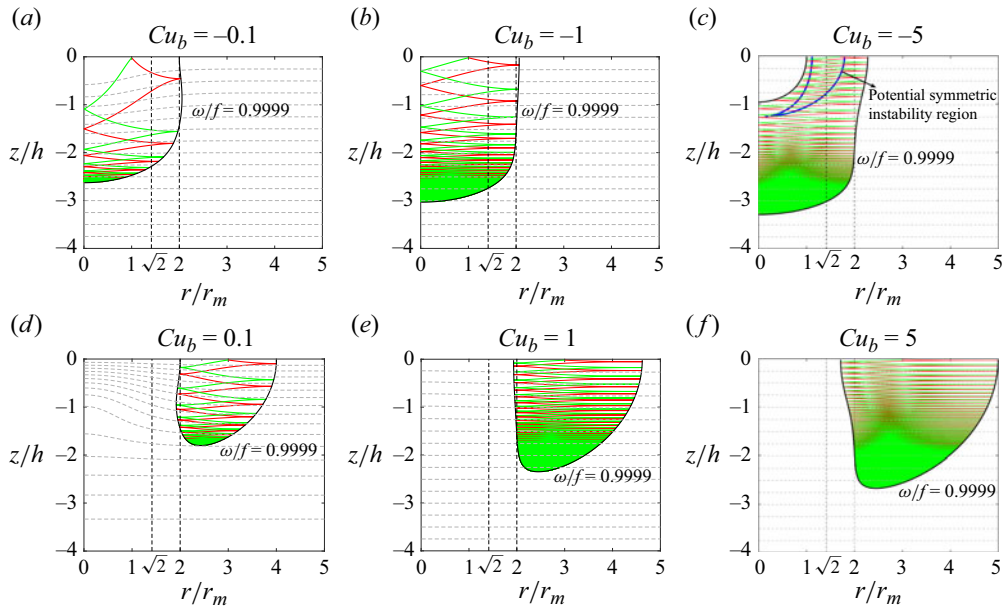
Figure 3. Downward-propagating rays (red and green curves) with frequency $\omega/f = 0.9999$, at different bulk curvature numbers Cu_b (*a*) -0.1 ($v_m = -0.5$ m s^{-1}, $r_m = 100$ km), (*b*) -1 ($v_m = -0.5$ m s^{-1}, $r_m = 10$ km), (*c*) -5 ($v_m = -0.75$ m s^{-1}, $r_m = 3$ km), (*d*) 0.1, (*e*) 1, and (*f*) 5. A solid black curve bounds the region of wave propagation. Grey dashed curves in the background denote isopycnals. For an anticyclonic vortex, $Cu_b < 0$, and for a cyclonic vortex, $Cu_b > 0$. Note that the region enclosed by blue curves in (*c*) indicates a possible symmetric instability region (see text for details).

scenario (dashed curves in figure 2), and vice versa. Also, for τ to be real, ω_0 should satisfy $\chi < \omega_0 < N$, giving the range of r that supports wave propagation. Further, in the straight front limit $Cu_b \to 0$, one can write $\chi^2 = f^2(1 + (4 - r^2/r_m^2) Cu_b \exp(-r^2/2r_m^2))$. For a given NIW frequency ω_0 (such that $\chi < \omega_0 < f$), the term $(4 - r^2/r_m^2) Cu_b$ should always be negative. As Cu_b is a negative number for the anticyclonic core case, the wave propagation region is bounded from above by $r/r_m = 2$, where $4 - r^2/r_m^2 = 0$. For an anticyclonic shield, the wave propagation region is bounded below by $r/r_m = 2$. In the purely geostrophic case, a similar analysis by neglecting $2\bar{v}/r$ in χ^2 reveals the critical radius as $r/r_m = \sqrt{2}$, i.e. the location where vorticity changes sign. This explains the contrasting behaviour of the wave propagation region due to curvature in both scenarios. Because the critical radius (at $z = 0$) is the same for both the anticyclonic core and shield, it indicates an increase in the region of wave propagation for the anticyclonic core, and a decrease in the wave propagation region for the anticyclonic shield, due to the inclusion of curvature terms (figure 2).

The effect of curvature is explored further by performing a ray-tracing study at various values of representative $|Cu_b|$ ($= 0.1, 1, 5$) as shown in figures 3(*a*)–3(*f*) for the anticyclonic core and shield, respectively. The isopycnals indicate a near-barotropic scenario at large $|Cu_b|$. A general conclusion from both sets of figures is that the region of wave propagation increases with an increase in $|Cu_b|$. Furthermore, the location of the critical layer depth, a location marked by vanishing vertical wavelengths, increases with the curvature number. However, note that at any Cu_b, not including the curvature terms underpredicts the critical layer depth in the anticyclonic core, and overpredicts it in the anticyclonic shield. Interestingly, for $Cu_b < -1$, a region of wave 'non-propagation' can
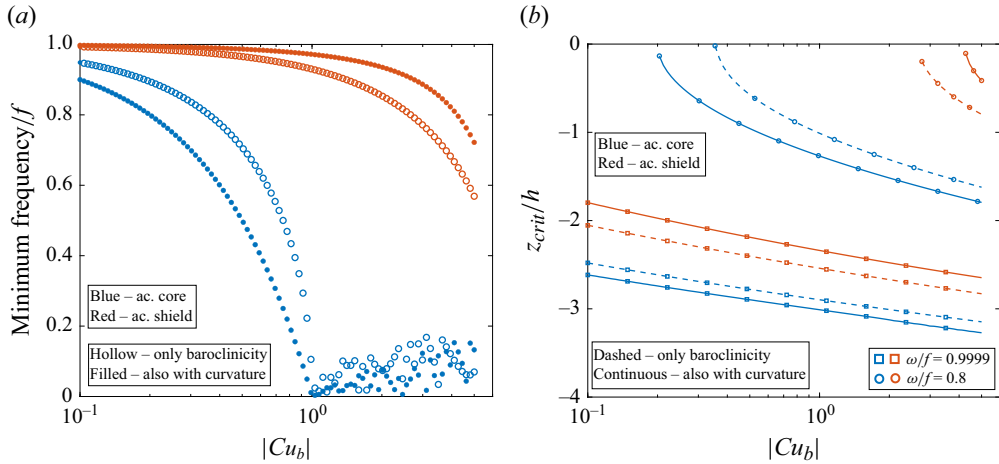
Figure 4. For an anticyclonic core (blue) and an anticyclonic shield (red), plotted as functions of curvature number magnitude ($|Cu_b|$) in a semi-log plot: (a) the minimum frequency that can be trapped, where hollow circles represent the scenario considering the geostrophic balance, whereas the filled circles show the scenario considering cyclogeostrophic balance; (b) the location of the critical layer (z_{crit}/h) for two different frequencies $\omega/f = 0.8$ (hollow circles) and 0.9999 (hollow squares). Dashed curves correspond to the scenario without curvature terms in the dispersion relation, while continuous curves correspond to the scenario with curvature terms.

be observed in the anticyclonic core, as shown in figure 3(c). This can be attributed to an increase in χ^2 above f^2, due to an increased contribution from the nonlinear term $(2\zeta\bar{v}/r)$ for $|Cu_b| > 1$. This results in the minimum allowable NIW frequency becoming super-inertial (i.e. more than f) near the vortex centre, in weakly baroclinic scenarios, therefore it cannot support trapping of NIWs until the vertical e-folding length (h). It is worth emphasising here the increase in NIW activity in the shield surrounding the anticyclonic core ($r > \sqrt{2}$), and a corresponding decrease in anticyclonic core ($r < \sqrt{2}$) for $z/h > -1$ in figure 3(c). Note that the region enclosed by blue curves in figure 3(c) corresponds to $\omega_{min}(r, z) < 0$, a necessary but not sufficient condition for symmetric instability (Buckingham *et al.* 2021a). It becomes a sufficient condition for parcel motions aligned with isopycnals, but as shown in (2.8), the slope of the group velocity vector cannot reach the isopycnal slope even at the boundaries of the wave propagation region (i.e. at $\omega_0 = \omega_{min}$). Finally, figure 3 shows that NIWs get trapped significantly below the vortex, albeit still in the anticyclonic core.

Figure 4(a) shows the minimum NIW frequency that can be trapped, plotted as a function of the curvature number magnitude. One observes that the NIW frequency band that is trapped increases with curvature number. In an anticyclonic core, including the curvature term reduces the lower limit of this band further. In an anticyclonic shield, however, the lower limit increases, allowing only a narrow band of NIWs to be trapped as $Cu_b \to 0$. In other words, the shields of cyclonic, approximately geostrophic vortices or straight fronts (i.e. small curvature) may not exhibit as appreciable NIW activity as their submesoscale or highly-curved counterparts.

Note, however, that (2.4) indicates that each NIW frequency stalls at a specific depth given by its critical layer. For an anticyclonic core, this can be derived analytically by noting that the critical layer occurs at $r = 0$ and $\omega_{min}(r = 0, z) = \chi(r = 0, z)$. Therefore, for a given frequency ω, the critical depth is given by $z_{crit}/h = -\sqrt{\ln(|Cu_b|/(1 - \omega/f))}$. In other words, the critical depth of an NIW increases with the curvature number, and

decreases with its separation from f. In figure 4(*b*), z_{crit}/h is plotted as a function of Cu_b, for two frequencies, $\omega = 0.8f$ – a typical lower-bound of NIW frequency band (e.g. Fer *et al.* 2018), and $\omega = 0.9999f$. In the anticyclonic shield, deriving an analytical expression for the critical depth z_{crit}/h is not as straightforward as it is for the anticyclonic core. However, the vertical location where a ray saturates (in other words, the critical depth) can be determined numerically using ray tracing. The increase in $|z_{crit}|$ with Cu_b for the anticyclonic shield is similar to the anticyclonic core. In contrast, considering the curvature terms (continuous curves) in the dispersion relation, for the anticyclonic shield, predicts a smaller z_{crit} compared to the case without curvature terms (dashed curves).

4. Discussion and conclusions

As mentioned in the Introduction, it is a common practice in the literature to use the expression $f_{eff} = f + \zeta/2$ to identify the trapping depth of NIWs, even in submesoscale flow features (Son *et al.* 2022). One of the main objectives of this work is to calculate the penalty of neglecting curvature in such flows that have typical curvature number of $O(1)$. Therefore, we consider two typical Arctic sub-surface eddies: (i) a shallow eddy in the Canada Basin (Son *et al.* 2022), and (ii) the Lofoten Basin Eddy (Fer *et al.* 2018). These vortices are chosen due to their high bulk curvature numbers. In contrast, for mesoscale eddies such as the Zapiola Anticyclone and the Cyprus Eddy (Zodiatis *et al.* 2005; Weijer *et al.* 2020) with $Cu_b \approx O(10^{-2})$, a significant increase in the trapping depth is not expected due to weak curvature effects. The CLM vortex is well suited as an idealised model in these scenarios. Note that the symmetry of the vortex model about the r-axis means that one can choose a non-zero z_0 to obtain a sub-surface eddy. For eddies (i) and (ii), we choose the parameters $\alpha = 4$ and 2, respectively, to maintain the core–shield vorticity ratio; other parameters, such as maximum azimuthal velocity and eddy radius, are obtained from Fer *et al.* (2018) and Son *et al.* (2022), respectively. Figure 5(*a*,*b*) show the ray paths and wave propagation boundaries for both the eddies. The results show that the trapping depth increases due to the curvature term. Specifically, increases of 18 % and 21 % of the vertical e-folding length are observed in eddies (i) and (ii), respectively. In addition, observations in both Fer *et al.* (2018) and Son *et al.* (2022) show that an increase in NIW activity is found at a location deeper than the critical depth obtained from their calculations. As presented here, frontal curvature can be a reason for this discrepancy. However, it has to be noted that the idealised models used here are indeed not perfect descriptions of the actual eddies, which are usually not axisymmetric, are present in a non-uniform background stratification, and may be evolving in time. Our future study aims to take these effects into account.

In this work, we have emphasised the role of frontal curvature in NIW trapping. We showed that curvature can act to increase the horizontal and vertical extents of the trapping regions in an anticyclonic core. In contrast, for a given cyclonic core vortex with an anticyclonic shield, the region of NIW activity reduces with the inclusion of curvature effects. The slope of energy propagation for NIWs in the curved front is larger than is predicted from the present-day geostrophic theory (Kunze 1985; Whitt & Thomas 2013) if the NIWs are present in the anticyclonic core, and smaller if they are present in the shield. Additionally, a non-trivial NIW non-propagation zone is observed in anticyclonic core regions at high curvatures, i.e. NIWs are trapped in an annulus around anticyclonic core vortices, although they stall in the core. By contrast, NIWs are trapped and stall in the anticyclonic annulus (shield) surrounding cyclonic vortices. Although the current
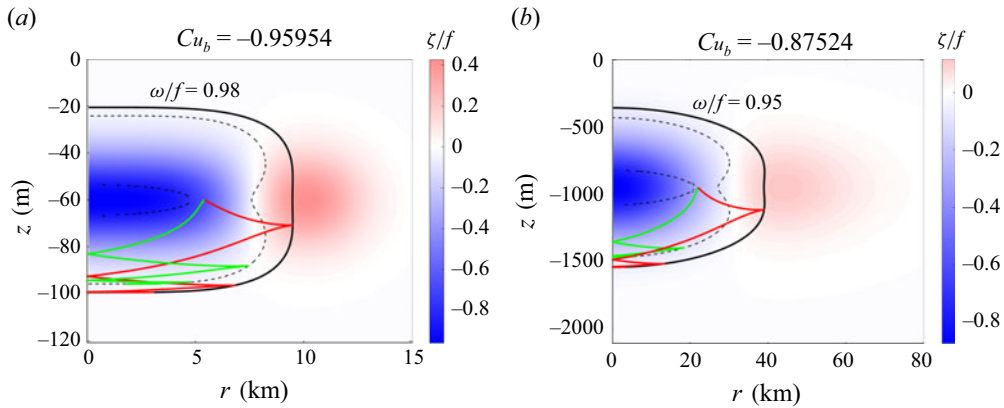
Figure 5. Idealised models of typical Arctic eddies: (*a*) a shallow eddy in the Canada Basin (Son *et al.* 2022); (*b*) the Lofoten Basin Eddy in the Norwegian Sea (Fer *et al.* 2018). The dashed black curves are wave propagation boundaries obtained without curvature terms, while the continuous black curves are wave propagation boundaries obtained with curvature terms. The leftward-propagating (green) curve is the ray corresponding to the scenario without the curvature term in the dispersion relation, while the rightward-propagating (red) curve is the ray corresponding to the scenario with the curvature term. The background contour plot describes the non-dimensional relative vorticity (ζ/f).

work considers the axisymmetric mode, the results stay qualitatively the same for the azimuthal mode -1 found in ocean observations. The main difference is that the frequency ω is now Doppler shifted by $-\bar{v}/r$. One can extend this study to realistic curved fronts and non-circular vortices as well. For example, in an elliptical vortex, our results imply that the trapping depth is the highest at the focal points and lowest at the centre of the vortex. Finally, we would like to emphasise the idealised nature of this study. Additional realistic features such as three-dimensional effects (e.g. variation in azimuthal direction), nonlinear interactions and wave-mean interactions alter the behaviour of NIW trapping and are currently being studied. Furthermore, the effects of frontal curvature on wave–eddy energetics in a submesoscale scenario need attention.

Appendix A. Numerical solution

In this appendix, we present the numerical solution of (2.1) and (2.2) to validate the ray-tracing results. Numerical viscosities have been added in u and w momentum equations to smooth errors at the grid scale. We follow the numerical scheme outlined by Whitt & Thomas (2013) for a highly baroclinic straight front. The governing equation (after simplification) is discretised using a fourth-order central difference scheme in a 200×200 grid. The zero streamfunction boundary conditions ($\psi = 0$) are implemented at the four ends of the domain. The right-hand and bottom boundaries are truncated at $r/r_m = 3$ and $z/h = 3$, respectively. After the numerical procedure, the energy density (E) is calculated

from the streamfunction (ψ), following Qu (2019):

$$E = \frac{\rho_0}{4\omega^2 r^2} \left((\chi^2 + \omega^2) |\psi_z|^2 + 2M^2 \psi_r^* \psi_z + N^2 |\psi_r|^2 \right), \tag{A1}$$

where the subscripts indicate differentiation with r and z, respectively. The contour plots of normalised energy density $\bar{E} = E/\max(E)$ are plotted for two cases of anticyclonic core vortices and one case of cyclonic core vortex, for NIW frequency $\omega = 0.99f$, in figures 1 and 2 of the supplementary material. Note that the background stratification is chosen to be $N_b = 100f, 150f$ in some cases to ease numerical evaluation, as higher background stratification requires a higher number of grid points to resolve the closely-spaced ray paths. For the small $|Cu_b|$ anticyclonic core case (see figure S1a of the supplementary material), a 100×100 grid seems to be sufficient, whereas the higher grid resolution mentioned earlier is needed for the high $|Cu_b|$ case (see figure S1b of the supplementary material) to resolve dense ray paths. A similar observation is also made for the cyclonic core vortices as well, where the ray paths are denser when compared to the anticyclonic scenario (see figure S2 of the supplementary material). The numerical viscosities implemented here are the same as used by Whitt & Thomas (2013). The plots show that there is a good match between the ray paths and the regions of maximum $\bar{E}$. Although the two upward-propagating rays are not shown in our ray-tracing calculation, they can be obtained and follow the additional red bands in figure S1a. The region of wave non-propagation is also clearly obtained as seen in figure S1b.

REFERENCES

ALFORD, M.H., MACKINNON, J.A., SIMMONS, H.L. & NASH, J.D. 2016 Near-inertial internal gravity waves in the ocean. *Annu. Rev. Mar. Sci.* **8** (1), 95–123.

ASSELIN, O. & YOUNG, W.R. 2019 An improved model of near-inertial wave dynamics. *J. Fluid Mech.* **876**, 428–448.

ASSELIN, O. & YOUNG, W.R. 2020 Penetration of wind-generated near-inertial waves into a turbulent ocean. *J. Phys. Oceanogr.* **50** (6), 1699–1716.

BENDER, C.M. & ORSZAG, S.A. 2013 *Advanced Mathematical Methods for Scientists and Engineers I: Asymptotic Methods and Perturbation Theory*. Springer Science & Business Media.

BRANNIGAN, L., MARSHALL, D.P., GARABATO, A.C.N., NURSER, A.J.G. & KAISER, J. 2017 Submesoscale instabilities in mesoscale eddies. *J. Phys. Oceanogr.* **47** (12), 3061–3085.

BUCKINGHAM, C.E., GULA, J. & CARTON, X. 2021a The role of curvature in modifying frontal instabilities. Part I: Review of theory and presentation of a nondimensional instability criterion. *J. Phys. Oceanogr.* **51** (2), 299–315.

BUCKINGHAM, C.E., GULA, J. & CARTON, X. 2021b The role of curvature in modifying frontal instabilities. Part II: Application of the criterion to curved density fronts at low Richardson numbers. *J. Phys. Oceanogr.* **51** (2), 317–341.

CARTON, X. & MCWILLIAMS, J.C. 1989 Barotropic and baroclinic instabilities of axisymmetric vortices in a quasigeostrophic model. In *Mesoscale/Synoptic Coherent Structures in Geophysical Turbulence* (ed. J.C.J. Nihoul & B.M. Jamart), vol. 50, pp. 225–244. Elsevier.

CONN, S., CALLIES, J. & LAWRENCE, A. 2025 Regimes of near-inertial wave dynamics. *J. Fluid Mech.* **1002**, A22.

ELIPOT, S., LUMPKIN, R. & PRIETO, G. 2010 Modification of inertial oscillations by the mesoscale eddy field. *J. Geophys. Res. Oceans* **115** (C9), C09010.

ESSINK, S., KUNZE, E., LIEN, R.C., INOUE, R. & ITO, S. 2022 Near-inertial wave interactions and turbulence production in a Kuroshio anticyclonic eddy. *J. Phys. Oceanogr.* **52** (11), 2687–2704.

FER, I., BOSSE, A., FERRON, B. & BOURUET-AUBERTOT, P. 2018 The dissipation of kinetic energy in the Lofoten Basin Eddy. *J. Phys. Oceanogr.* **48** (6), 1299–1316.

GERTZ, A. & STRAUB, D.N. 2009 Near-inertial oscillations and the damping of midlatitude gyres: a modeling study. *J. Phys. Oceanogr.* **39** (9), 2338–2350.

GILL, A.E. 1984 On the behavior of internal waves in the wakes of storms. *J. Phys. Oceanogr.* **14** (7), 1129–1151.

JOYCE, T.M., TOOLE, J.M., KLEIN, P. & THOMAS, L.N. 2013 A near-inertial mode observed within a Gulf Stream warm-core ring. *J. Geophys. Res.: Oceans* **118** (4), 1797–1806.

KAFIABAD, H.A., VANNESTE, J. & YOUNG, W.R. 2021 Interaction of near-inertial waves with an anticyclonic vortex. *J. Phys. Oceanogr.* **51** (6), 2035–2048.

KAWAGUCHI, Y., YABE, I., SENJYU, T. & SAKAI, A. 2023 Amplification of typhoon-generated near-inertial internal waves observed near the Tsushima oceanic front in the Sea of Japan. *Sci. Rep.* **13** (1), 8387.

KLEIN, P. & SMITH, S.L. 2001 Horizontal dispersion of near-inertial oscillations in a turbulent mesoscale eddy field. *J. Marine Res.* **59** (5).

KLEIN, P. & TREGUIER, A.M. 1994 Dispersion of wind-induced internal waves by a barotropic jet. *J. Marine Res.* **53** (1).

KUNZE, E. 1985 Near-inertial wave propagation in geostrophic shear. *J. Phys. Oceanogr.* **15** (5), 544–565.

KUNZE, E., SCHMITT, R.W. & TOOLE, J.M. 1995 The energy balance in a warm-core ring's near-inertial critical layer. *J. Phys. Oceanogr.* **25** (5), 942–957.

LEE, D. & NIILER, P.P. 1998 The inertial chimney: the near-inertial energy drainage from the ocean surface to the deep layer. *J. Geophys. Res.: Oceans* **103** (C4), 7579–7591.

LELONG, M.-P., CUYPERS, Y. & BOURUET-AUBERTOT, P. 2020 Near-inertial energy propagation inside a Mediterranean anticyclonic eddy. *J. Phys. Oceanogr.* **50** (8), 2271–2288.

LIGHTHILL, J. 2001 *Waves in Fluids*. Cambridge University Press.

LLEWELLYN SMITH, S.G. 1999 Near-inertial oscillations of a barotropic vortex: trapped modes and time evolution. *J. Phys. Oceanogr.* **29** (4), 747–761.

MAHDINIA, M., HASSANZADEH, P., MARCUS, P.S. & JIANG, C.H. 2017 Stability of three-dimensional Gaussian vortices in an unbounded, rotating, vertically stratified, Boussinesq flow: linear analysis. *J. Fluid Mech.* **824**, 97–134.

MUNK, W. & WUNSCH, C. 1998 Abyssal recipes II: Energetics of tidal and wind mixing. *Deep Sea Res. I: Oceanogr. Res. Papers* **45** (12), 1977–2010.

NIRANJAN KUMAR, K., RAO, C.K., SANDEEP, A. & RAO, T.N. 2014 SODAR observations of inertia-gravity waves in the atmospheric boundary layer during the passage of tropical cyclone. *Atmos. Sci. Lett.* **15** (2), 120–126.

PERKINS, H. 1976 Observed effect of an eddy on inertial oscillations. In *Deep Sea Research and Oceanographic Abstracts*, vol. 23, pp. 1037–1042. Elsevier.

QU, L. 2019 Submesoscale vortices and near-inertial waves in coastal buoyancy-driven flow . PhD thesis, Texas A&M University.

SERAFIMOVICH, A., HOFFMANN, P., PETERS, D. & LEHMANN, V. 2005 Investigation of inertia-gravity waves in the upper troposphere/lower stratosphere over northern Germany observed with collocated VHF/UHF radars. *Atmos. Chem. Phys.* **5** (2), 295–310.

SHAKESPEARE, C.J. 2016 Curved density fronts: cyclogeostrophic adjustment and frontogenesis. *J. Phys. Oceanogr.* **46** (10), 3193–3207.

SNYDER, C., MURAKI, D.J., PLOUGONVEN, R. & ZHANG, F. 2007 Inertia–gravity waves generated within a dipole vortex. *J. Atmos. Sci.* **64** (12), 4417–4431.

SOLBERG, M. 1936 Le mouvement d'inertie de l'atmosphere stable et son role dans le theorie des cyclones. *Sixth Assembly, Paul Dupont, Edinburgh, Union Geodesique et Geophysique Internationale*, pp. 66–82.

SON, E.Y., KAWAGUCHI, Y., COLE, S.T., TOOLE, J.M. & HA, H.K. 2022 Assessment of turbulent mixing associated with eddy–wave coupling based on autonomous observations from the Arctic Canada Basin. *J. Geophys. Res.: Oceans* **127** (9), e2022JC018489.

TAYLOR, S. & STRAUB, D. 2020 Effects of adding forced near-inertial motion to a wind-driven channel flow. *J. Phys. Oceanogr.* **50** (10), 2983–2996.

THOMAS, J. & ARUN, S. 2020 Near-inertial waves and geostrophic turbulence. *Phys. Rev. Fluids* **5** (1), 014801.

THOMAS, J. & DANIEL, D. 2021 Forward flux and enhanced dissipation of geostrophic balanced energy. *J. Fluid Mech.* **911**, A60.

THOMAS, J., SMITH, K.S. & BÜHLER, O. 2017 Near-inertial wave dispersion by geostrophic flows. *J. Fluid Mech.* **817**, 406–438.

VOET, G. 2024 Near-inertial energy variability. *Oceanography* **37** (4), 34–47.

WANG, S., ZHANG, F. & SNYDER, C. 2009 Generation and propagation of inertia–gravity waves from vortex dipoles and jets. *J. Atmos. Sci.* **66** (5), 1294–1314.

WEIJER, W., BARTHEL, A., VENEZIANI, M. & STEINER, H. 2020 The Zapiola Anticyclone: a Lagrangian study of its kinematics in an eddy-permitting ocean model. *Deep Sea Res. I: Oceanogr. Res. Papers* **164**, 103308.

WHITT, D.B. & THOMAS, L.N. 2013 Near-inertial waves in strongly baroclinic currents. *J. Phys. Oceanogr.* **43** (4), 706–725.

WHITT, D.B. & THOMAS, L.N. 2015 Resonant generation and energetics of wind-forced near-inertial motions in a geostrophic flow. *J. Phys. Oceanogr.* **45** (1), 181–208.

WUNSCH, C. & FERRARI, R. 2004 Vertical mixing, energy, and the general circulation of the oceans. *Annu. Rev. Fluid Mech.* **36** (1), 281–314.

XU, X., ZHAO, W., HUANG, X., HU, Q., GUAN, S., ZHOU, C. & TIAN, J. 2022 Observed near-inertial waves trapped in a propagating anticyclonic eddy. *J. Phys. Oceanogr.* **52** (9), 2029–2047.

YOUNG, W.R. & BEN JELLOUL, M. 1997 Propagation of near-inertial oscillations through a geostrophic flow. *J. Mar. Res.* **55** (4), 735–766.

ZODIATIS, G., DRAKOPOULOS, P., BRENNER, S. & GROOM, S. 2005 Variability of the Cyprus warm core eddy during the CYCLOPS project. *Deep Sea Res. II: Topical Studies Oceanogr.* **52** (22–23), 2897–2910.